A Versatile G-quadruplex (G4)-coated Upconverted Metal-Organic Framework for Hypoxic Tumor Therapy

Xuanxiang Mao, Xiaobo Zhang, Zhicong Chao, Dehui Qiu, Shijiong Wei, Rengan Luo, Desheng Chen, Yue Zhang, Yun Chen, Yuanjiao Yang, et al.

A Versatile G-Quadruplex (G4)-Coated Upconverted Metal-Organic Framework for Hypoxic Tumor Therapy

Xuanxiang Mao, Xiaobo Zhang, Zhicong Chao, Dehui Qiu, Shijiong Wei, Rengan Luo, Desheng Chen, Yue Zhang, Yun Chen, Yuanjiao Yang, David Monchaud, Huangxian Ju, Jean-Louis Mergny, Jianping Lei, and Jun Zhou**

Given the complexity of the tumor microenvironment, multiple strategies are being explored to tackle hypoxic tumors. The most efficient strategies combine several therapeutic modalities and typically requires the development of multifunctional nanocomposites through sophisticated synthetic procedures. Herein, the G-quadruplex (G4)-forming sequence AS1411-A (d[$(G_2T)_4TG(TG_2)_4A$]) is used for both its anti-tumor and biocatalytic properties when combined with hemin, increasing the production of O_2 ca. two-fold as compared to the parent AS1411 sequence. The AS1411-A/hemin complex (GH) is grafted on the surface and pores of a core-shell upconverted metal-organic framework (UMOF) to generate a UMGH nanoplatform. Compared with UMOF, UMGH exhibits enhanced colloidal stability, increased tumor cell targeting and improved O_2 production (8.5-fold) in situ. When irradiated by near-infrared (NIR) light, the UMGH antitumor properties are bolstered by photodynamic therapy (PDT), thanks to its ability to convert O_2 into singlet oxygen ($^1O_2$). Combined with the antiproliferative activity of AS1411-A, this novel approach lays the foundation for a new type of G4-based nanomedicine.

X. Mao, X. Zhang, Z. Chao, D. Qiu, S. Wei, R. Luo, D. Chen, Y. Chen, Y. Yang, H. Ju, J.-L. Mergny, J. Lei, J. Zhou
State Key Laboratory of Analytical Chemistry for Life Science
School of Chemistry and Chemical Engineering
Nanjing University
Nanjing 210023, P. R. China
E-mail: jean-louis.mergny@inserm.fr; jun.zhou@nju.edu.cn

Y. Zhang
School of Pharmacy
Nanjing University of Chinese Medicine
Nanjing 210023, P. R. China

D. Monchaud
Institut de Chimie Moléculaire (ICMUB)
CNRS UMR6302
uB
Dijon 21078, France

J.-L. Mergny
Laboratoire d'Optique et Biosciences (LOB)
Ecole Polytechnique
CNRS
INSERM
Institut Polytechnique de Paris
Palaiseau 91120, France

1. Introduction

G-Quadruplexes (G4s) are four-stranded structures formed by guanine (G)-rich strands which have emerged as a subject of intense interest in fields as diverse as cell biology, chemical biology, and bionanotechnology.[1] G4-forming sequences are abundantly present in both the human genome and transcriptome, thereby making them a popular target for genetic research in order to decipher their cellular functions.[2] G4s have also been used to create nanodevices, which have been effectively implemented as artificial enzymes, biosensors, and drug carriers.[3] For instance, several G4 aptamers such as AS1411,[4] TBA,[5] apMNK,[6] S13,[7] S50,[7] and AT11[8a] have been reported to interact with cellular targets, resulting in therapeutic effects through various mechanisms, one example being the inhibition of the expression of the anti-apoptotic protein B-cell lymphoma 2 (Bcl-2).[4b,8b–d] These G4 aptamers display desirable characteristics such as easy chemical access and modification, high cellular uptake and serum stability, and low immunogenicity.[9] Although G4 aptamers exhibit interesting target specificity and potential therapeutic activity,[4–9] their application is limited due to the complex tumor microenvironment, which makes them difficult to deploy in a standardized manner. To address this challenge, we report here on the design, synthesis and use of a multifunctional nanomaterial as an efficient theranostic agent.

Nanomaterials such as metal-based nanospheres, carbon nanotubes, and metal-organic frameworks (MOFs)[10] functionalized with DNAs are gaining widespread interest in nanobiotechnology. MOFs in particular are interesting nanocarriers owing to their easy synthetic access, controllable pore size, large specific surface area, low cytotoxicity and good biocompatibility, making them suitable for drug delivery, catalysis and biosensing applications.[3b,11] Moreover, by coating them with G4-forming aptamers such as AS1411, MOFs can be specifically driven to cancer cells through the interaction between aptamers and cell-surface G4-affinic receptors, such as nucleolin.[12] Porphyrinic MOFs can even be used in photodynamic therapy (PDT) as they enable increasing loading of photosensitizers (PSs).[13] However, a limitation to the broader use of PDT with

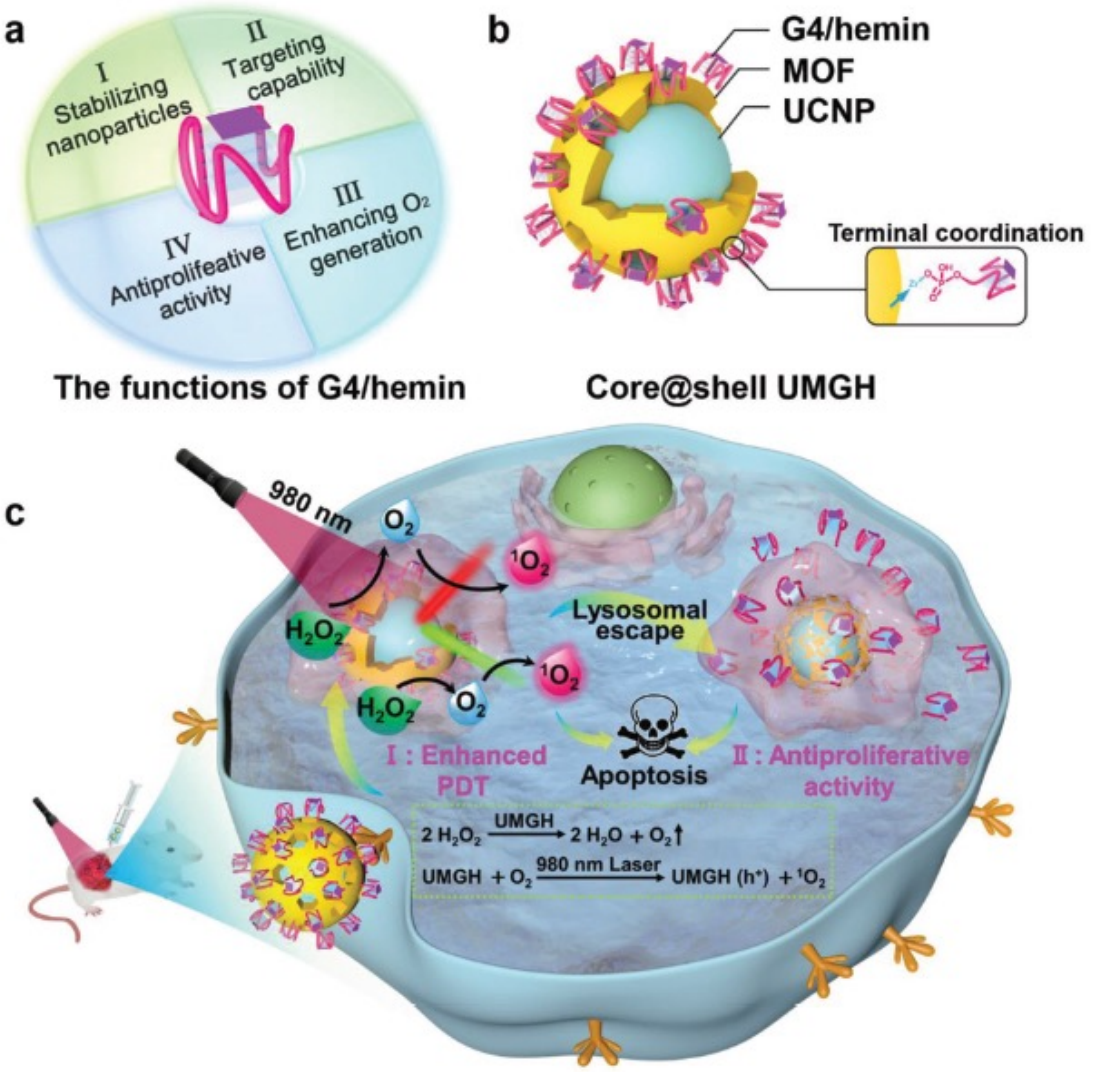

Scheme 1. Schematic illustration of a) the roles of G4/hemin (GH) complexes in the present work, b) the core-shell UMGH nanoplatform, and c) the antitumor mechanism of the UMGH nanoplatform. Hemin is represented as a purple square, and G-quadruplex/hemin is expressed as G4/hemin (GH); UCNP stands for upconversion luminescence nanoparticle, MOF for metal-organic framework, and the GH-functionalized core-shell UCNP@MOF is referred to as UMGH.

porphyrin-based MOFs lies in the necessity of visible light activation, which restricts tissue penetration. To overcome this problem, near-infrared (NIR) light irradiation would be a preferable option, thanks to its deeper tissue penetration and lower induced tissue damage.[14] Consequently, upconversion luminescence nanoparticles (UCNPs) are viewed as the best option for converting NIR light to the visible spectrum, thus enabling NIR-promoted PDT through fluorescence resonance energy transfer (FRET) between UCNP and MOFs.[15] However, the efficiency of O_2-dependent PDT is hindered by the highly hypoxic microenvironment found in solid tumors.[16]

To produce O_2 in situ, nanomaterial-based catalysts employing either natural (e.g., catalase) or artificial enzymes (e.g., nanozymes) are commonly used since they are capable of producing O_2 in areas with high concentrations of H_2O_2 such as tumors.[17a,b] The use of catalase, in spite of its high efficiency for the conversion of H_2O_2 into O_2 in tumor tissues, is limited by its physiological instability.[17c] Nanozymes, such as ion-doped nanozymes (Fe^{III}-C_3N_4 nanosheets),[17d] composite nanozymes (Prussian blue),[17e] MOF nanozymes (MIL-100 (Fe))[17f] and precious metal nanozymes (Pt, Au@Rh),[17g,h] offer higher efficiencies but their synthesis and colloidal stability are limiting. Recently, the Liu group developed a polymer comprising AS1411, hemin and chlorin e6 (Ce6), which can effectively convert tumor endogenous H_2O_2 into O_2, thereby mimicking catalase, which proved to be effective for PDT.[18]

This system has a great potential for further improvements; we have thus taken the best elements from these approaches to design an optimized nanotool. As seen in **Scheme 1**, we designed and constructed a G4 aptamer termed AS1411-A (d[$(G_2T)_4TG(TG_2)_4A$]), derived from AS1411, which has already entered clinical trials for cancer therapy.[4c,d,9a] While preserving the attractive properties of AS1411 (i.e., targeting cancer cells, stabilizing nanoparticles, displaying interesting antiproliferative activity), AS1411-A exhibited a substantially increased efficiency in converting H_2O_2 to O_2 in the presence of hemin when compared to AS1411 (further elaborated on below). Then, we anchored the AS1411-A/hemin (GH) complex on the surface and pores of the core-shell UCNP@porphyrinic MOF (referred to as UMGH), in the aim of using this construct to fight hypoxic

tumors via a combined action of enhanced PDT and antiproliferative activities. Upon irradiation at 980 nm (NIR region), a FRET phenomenon enabled the sensitization of the porphyrinic MOF, resulting in the generation of singlet oxygen ($^1O_2$). This PDT activity, when combined with the anticancer activity of AS1411-A, created a nanoplatform with a very high efficiency against hypoxic tumors, as demonstrated here both in vitro and in vivo. These findings thus broaden the possible use of G4s in the oncology field, as the UMGH system described hererepresents a novel type of theranostics agents.

2. Results and Discussion

2.1. Synthesis and Characterization of UMGH NPs

We synthesized the core-shell upconverted metal-organic framework (UMOF) with an individual UCNP as the core and porphyrin MOF as the shell, using a heterogeneous nucleation approach.[19] We then functionalized the UMOF with the GH complex through a simple coordination approach between the terminal phosphate of the G4 and tan unsaturated Zr sites in the UMOF (**Figure 1**a). In more detail, the initial core of the uniform UCNP was stabilized by oleic acid (OA-UCNP) with an average size distribution of ca. 29 nm, as evaluated by powder X-ray diffraction (PXRD) and transmission electron microscopy (TEM) imaging (Figure S1, Supporting Information). We removed the oleic acid with nitrosonium tetrafluoroborate ($NOBF_4$),[20] then coated the surface of the UCNP with 3,4-dihydroxyhydrocinnamic acid (DHCA) to form DHCA-UCNP (Figure 1b) and PCN-222, combining tetrakis (4-carboxyphenyl) porphyrin (H_2TCPP) with metal ions (Zr(IV)).[19] As Zr(IV) tended to adsorb on the surface of DHCA-UCNP by virtue of the strong interaction with the carboxylic acid groups of DHCA-UCNP, nucleation and growth of Zr MOF was conducted on the surface of the DHCA-UCNP for the formation of core-shell UCNP@MOF heterostructures (UMOF). As shown in Figure 1c, TEM indicated an average diameter of ≈59 nm with a ≈100% encapsulation efficiency for the UMOF. Scanning electron microscopy (SEM) and elemental mapping demonstrated a uniform distribution of elements (Y, Yb, and Zr) within the core-shell nanospheres (Figure S2, Supporting Information).

Next, the core-shell UMOF with coordinatively unsaturated metal sites were functionalized with terminal phosphate-modified GH to form core-shell UMGH.[21] An excess of GH was added to the dispersed UMOF and incubated for 24 h at room temperature. The GH loading efficiency was evaluated by UV–vis absorbance changes in the supernatant before and after functionalization using the corresponding calibration curve of G4 (Figure S3, Supporting Information). This efficiency was determined to be as high as 4.01 ± 0.26 wt %, indicative of higher loading capacity than our previous system based on MIL-53 (Fe).[3b] TEM and SEM analyses confirmed the core-shell geometry of UMGH (Figure 1d; Figure S4, Supporting Information). A PXRD analysis further established that the crystalline structure UMOF was unaffected by GH functionalization (Figure S5, Supporting Information).[22] Both energy dispersive X-ray elemental mapping and EDS line scan of UMGH showed that Yb, Zr, P, and Fe elements were homogeneously distributed throughout the core-shell spheres (Figures 1e and Figure S6, Supporting Information) testifying to the presence of two additional elements (P and Fe) belonging to the GH complex (Scheme 1b). Further verification of the proper formation of UMGH was provided by Fourier-transform infrared (FT-IR) analyses of GH, UMOF and UMGH. As shown in Figure S7 (Supporting Information), UMOF-containing samples displayed the characteristic peaks of Zr—O bond (655 cm^{-1}),[23a,b] and GH-containing samples showed a peak at 1056 cm^{-1} corresponding to the C-N group of hemin,[23c] thereby confirming the successful formation of UMGH.

Further information about the UMOF/GH interaction was obtained through photoelectron spectroscopy (XPS) measurements: as seen in Figure 1f, XPS analyses demonstrated the presence of C, Zr, and O elements within the UMOF, and of two additional elements (P and Fe) in UMGH, confirming that GH complexes were efficiently grafted on the outer surface of the UMOF. In more detail, the typical P peak (2p, 134.3 eV) was absent in UMOF and present in UMGH (Figure 1g), indicative of the addition of GH on UMOF. Compared to UMOF, the Zr (3d) peak of UMGH underwent a redshift due to the greater electronegativity of P as compared to Zr and the formation of a Zr—O—P bond between G4 and UMOF that weakens the density of the electron cloud around Zr atoms (Figure S8a, Supporting Information), leading to a decrease in the shielding effect on external electrons, thus boosting the binding energy of internal electrons.[24] The O (1s) peak in UMGH further proved the GH/UMOF connection through P—O—Zr bond (531.3 eV) (Figure 1h).[24] In addition, the interactions between UMOF and tripolyphosphate (STPP) were compared and analyzed because Zr MOFs could form Zr—O—P bonds with inorganic phosphates.[24] As shown in Figure S8b (Supporting Information), similar variations of O (1s) peaks indicated that GH binds to UMOF through Zr—O—P bonds. Finally, the Fe (2p) spectrum was analyzed (Figure S8c, Supporting Information), displaying peaks at 710.6, 716.8, 711.2, and 725.1 eV, which were attributed to Fe^0 $2p_{3/2}$, Fe^0 $2p_{1/2}$, Fe-N $2p_{3/2}$, and Fe-N $2p_{1/2}$, respectively, thus implying the presence of hemin within UMGH.[22b,25]

To further characterize the surface area and pore size of both UMOF and UMGH, the nitrogen adsorption–desorption isotherm was measured: as seen in Figure 1i, the Brunauer-Emmett-Teller (BET) surface area decreased from unfunctionalized UMOF (1976 $m^2\ g^{-1}$) to UMGH (984 $m^2\ g^{-1}$), which was attributed to the GH loading within the pores of UMOF. Additionally, their pore size distributions were ≈27 Å, and the pore volume of UMGH decreased markedly, suggesting partial pore filling by GH complexes (Figure S9a, Supporting Information). These results, together with previous XPS data, indicated that GH complexes are present on the surface as well as within the pores of UMOFs, where their activity is still possible. Additionally, the zeta (ζ) potentials of UCNP, UMOF and UMGH (Figure 1j) were +24.7, +11.1 and −33.9 mV, respectively, indicating a better dispersion of UMGH in aqueous solution compared to UCNP and UMOF.[26] Dynamic light scattering (DLS) measurements showed that UMGH had a larger hydrophilic diameter than UMOF (122 nm vs 105 nm), which again confirmed the GH loading on the surface of UMOF (Figure 1k). After a 5-h incubation in an aqueous solution, DLS analyses showed that UMGH exhibited a lower polydispersity (index = 0.281) than UMOF (0.603), proving that GH increased the colloidal stability of UMOF. Moreover,

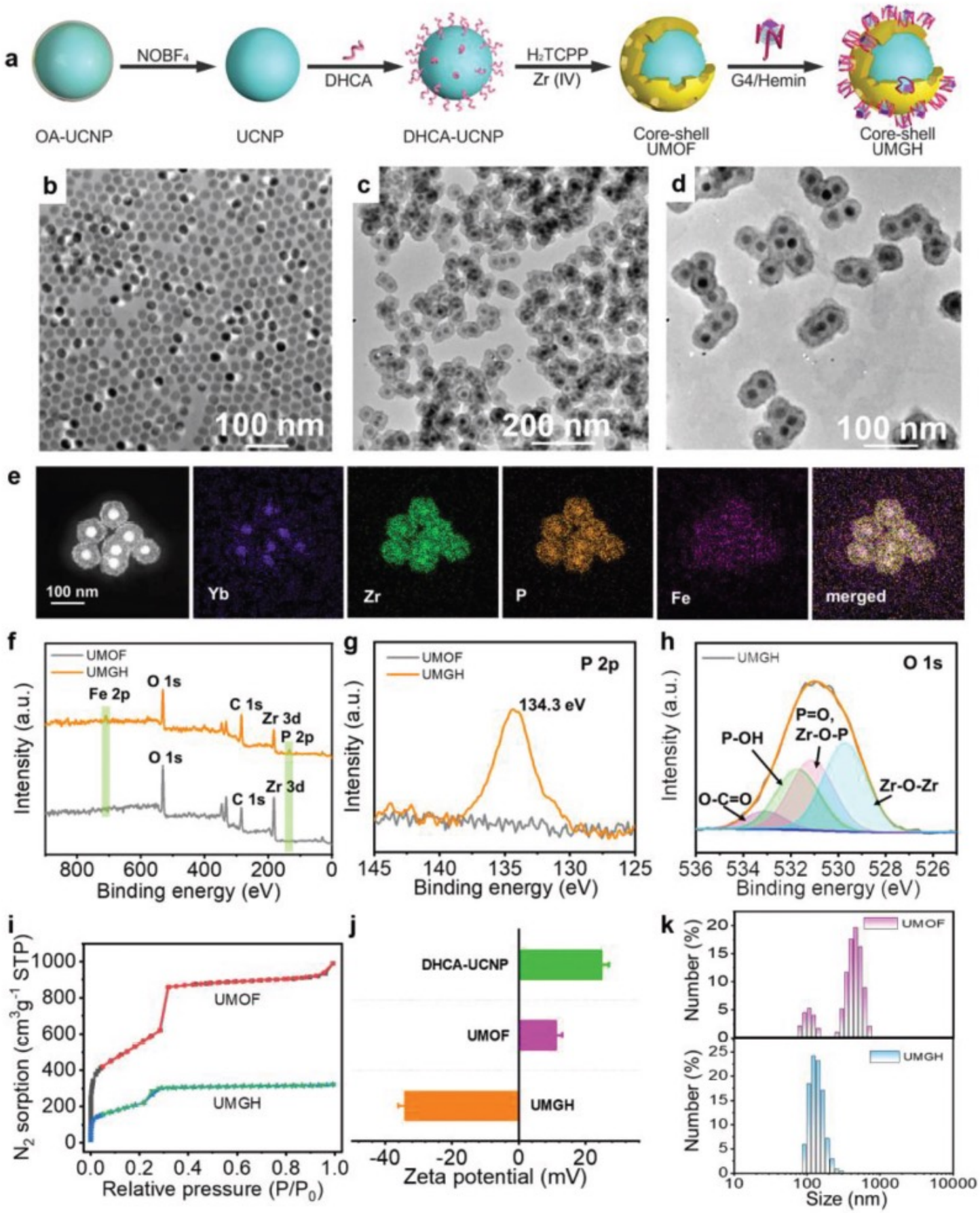

Figure 1. Preparation and characterization of UMGH nanostructures. a) Schematic illustration of the synthesis of core-shell UMGH starting from oleic acid-capped UCNP (OA-UCNP). b–d) TEM images of (b) DHCA-UCNP, (c) core-shell UMOF and (d) core-shell UMGH. e) Energy dispersive X-ray elemental mapping of UMGH. f) Photoelectron spectroscopy (XPS) spectra of UMOF before and after modification with GH. g,h) High-resolution XPS spectra of (g) P 2p and (h) O 1s. i) N_2 adsorption and desorption isotherms for UMOF and UMGH. j) Zeta (ζ) potential of DHCA-UCNP, UMOF, and UMGH. k) Dynamic light scattering (DLS) size distribution of UMOF and UMGH in aqueous solution (5-h incubation).

no obvious change in UMGH hydrophilic diameter was notable in aqueous solution after one week (Figure S9b, Supporting Information), thus confirming its very high stability. Collectively, these results demonstrated the successful synthesis of the core-shell UMGH nanoplatform, with GH complexes being present both on the surface and inside the pores of the UMOF.

2.2. The Functionality of G4/Hemin Complex

We then decided to further investigate and optimize the catalytic activity of GH complexes. We first verified that GH complexes could indeed catalyze the decomposition of H_2O_2 to produce O_2, as previously reported.[18,27] In an effort to enhance the catalytic performance of GH complexes, we optimized the nature of the G4 core (**Figure 2**a). To this end, we studied a series of AS1411 derivatives with different terminal base compositions (Table S1, Supporting Information). Circular dichroism (CD) analyses confirmed their G4 structures (Figure S10, Supporting Information).[28a] As seen in Figure 2b and Figure S11 (Supporting Information), the catalytic activities of all AS1411 derivatives (associated with hemin) were found to be significantly enhanced in comparison to the original AS1411. Amongst them, AS1411-A, which had an additional A base at its 3′ end, was the most active: its initial velocity (V_0) of oxygen production from 2 mM H_2O_2 increased to 0.13 mg L^{-1} s^{-1}, being almost two-fold higher than that of AS1411 (V_0 = 0.07 mg L^{-1} s^{-1}). The catalytic activity was further analyzed by varying the H_2O_2 concentration: the results seen in Figure 2c revealed that the V_0 increased with the H_2O_2 concentration and that AS1411-A has a superior catalytic activity to AS1411. The catalytic mechanism explaining the production of O_2 relies on the oxidation of hemin bound to G4 by H_2O_2 to form compound I (Fe^{IV}=OPor^{+}), which further reacts with another molecule of H_2O_2 to produce O_2 and H_2O, and regenerates the pseudo-enzyme.[28b]

Next, the antiproliferative activities of AS1411 and derivatives on both no-ncancerous (MCF-10A) and cancerous cells (mouse triple-negative breast cancer cell line 4T1) were assessed using the colorimetric methylthiazolyltetrazolium (MTT) assay. The results showed negligible effects on the survival of MCF-10A cells (Figure 2d) whereas AS1411 derivatives elicited strong dose-dependent cytotoxic effects on 4T1 cells (Figures 2e,f; Figure S12, Supporting Information). The IC_{50} values of AS1411 derivatives were close to that of AS1411 (Table S2, Supporting Information). To further analyze the ability of AS1411 and AS1411-A to induce cell apoptosis, the apoptotic profile of 4T1 cells with annexin V-FITC/PI double staining was assessed by flow cytometry. Similar results were obtained for both AS1411 and AS1411-A, with a proportion of apoptotic cells (the sum of early and late apoptotic cells) of 53.9 and 51.3%, respectively, after 96-h incubation at 10 μM concentration (Figure 2g).

Finally, we verified that AS141-1A efficiently targets 4T1 cells by optical imaging (confocal laser scanning microscope, CLSM) using a FAM-labeled aptamer. As seen in Figure 2h, the ability of AS1411-A to interact with cancer cells was illustrated by the strong green fluorescence of the treated 4T1 cells. Collectively, these data demonstrate that the AS1411-A/hemin complex catalyzes the degradation of H_2O_2 to produce O_2, stabilizes UMOF in aqueous solution, targets and triggers apoptosis of 4T1 cells.

2.3. The Multifunctional UMGH

The functionality of UMGH was investigated through a cascade catalysis process. This process consisted of two steps, the first being the production of O_2 from H_2O_2 and the second being the FRET-mediated production of $^1O_2$ from O_2. To assess the ability of UMGH to convert H_2O_2 into O_2, the amount of O_2 produced by either UMOF or UMGH was measured in solution. As seen in **Figure 3**a, the dissolved O_2 produced by UMGH increased to 5.88 mg L^{-1} in 300 s, which was 8.5 times higher than the amount produced by UMOF. This noteworthy difference confirmed the role of the grafted GH in O_2 generation, and was further corroborated by the noticeable O_2 bubbling observed after the addition of UMGH (Figure S13, Supporting Information).

Next, the energy transfer ability of UMGH was investigated. Under NIR light irradiation (980 nm), the UCNP core harvested low-energy photons and exhibited a relatively broad upconversion luminescence (UCL) emission in the range of 510–565 nm ($^2H_{11/2}$, $^4S_{3/2}$ → $^4I_{15/2}$) and 650–675 nm ($^4F_{9/2}$ → $^4I_{15/2}$).[29] This emission aligned with the Q bands (500–700 nm) of the outer porphyrin MOF shells, suggesting a potential energy transfer from the UCNP core to the porphyrin MOF shell (Figure S14, Supporting Information). Subsequently, the UCL spectra of the UCNP, UMOF, and UMGH were measured and analyzed (Figure 3b): like UMOF, the emission bands of UMGH suggested an efficient energy transfer from the inner UCNP core to the outer porphyrin MOF shell. To confirm this energy transfer, time-resolved photoluminescence measurements were conducted: as seen in Figure S15 (Supporting Information), the UCL decay curves of UCNP and UMGH showed an obvious reduction from 161 to 94 μs after GH grafting, which can be used to estimate the energy transfer efficiency from UCNP core to the shell within UMGH, which is ca. 42% according to previously described calculation methods.[22]

We then determined the effectiveness of UMGH to produce $^1O_2$ upon NIR irradiation (980 nm). To this end, we employed the singlet oxygen sensor green (SOSG) reagent to monitor $^1O_2$ production by the porphyrin MOF, under both normoxia and hypoxia conditions, with or without laser illumination (0.5 W cm^{-2}). As seen in Figure 3c, with UMGH in normoxia conditions, low and high $^1O_2$ production was detected before and after 980 nm laser irradiation, respectively, indicating that light is an active trigger for $^1O_2$ production. This generation was much higher than that of MGH (G4/hemin anchored Zr MOF), demonstrating the efficient energy transfer between the UCNP core and the porphyrinic MOF shell. The $^1O_2$ generation of UMGH decreased to 11% under hypoxia conditions (constant N_2 flush), which could be reversed by the addition of H_2O_2 (100 μM), confirming the strong catalytic activity of UMGH to decompose H_2O_2 into O_2. The $^1O_2$ quantum yield ($\Phi_{\Delta(x)}$) of UMGH was determined to be 0.31 using methylene blue (MB) as a standard (Figure S16, Supporting Information).[30] Additionally, electron spin resonance (ESR) experiments were conducted to confirm the production of $^1O_2$ and $O_2^{\bullet-}$ upon exposure to NIR light: as seen in Figure 3d, three characteristic peaks (1:1:1 ratio) were observed in the presence of 2,2,6,6-tetramethyl-4-piperidine (TEMP) to trap $^1O_2$ in water under continuous N_2 flush and upon irradiation at 980 nm for 30 min in the presence of 100 μM H_2O_2. This result was close to the signals detected in normoxia conditions with either

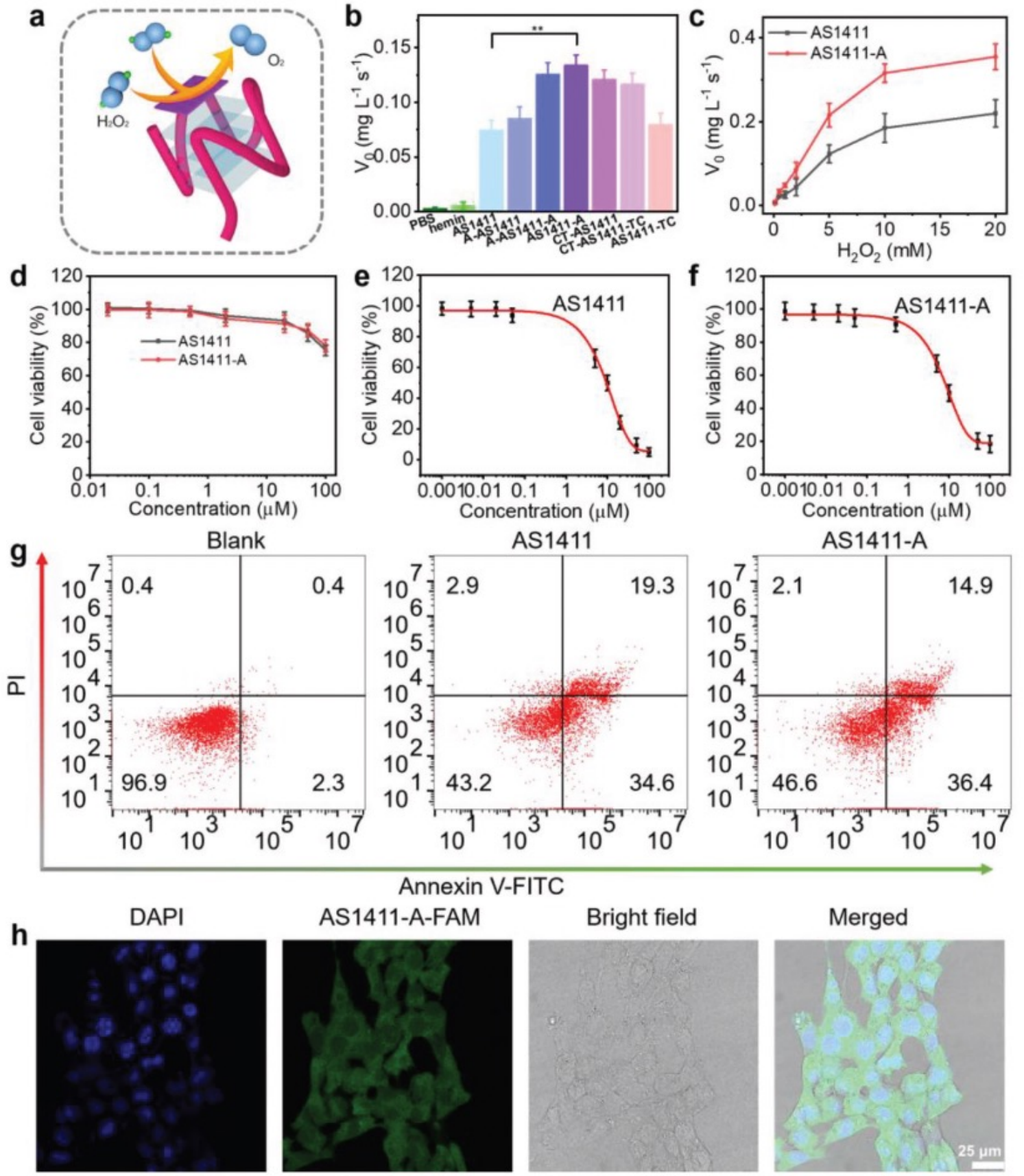

Figure 2. Properties of AS1411-A/hemin complexes. a) Schematic illustration of the conversion of H_2O_2 into O_2 by GH complexes. b) Initial velocity (V_0) of oxygen production in 2.0 mM H_2O_2 solutions after adding a series of AS1411 derivatives in interaction with hemin. $^{**}p < 0.01$. c) Relationship between initial velocity (V_0) of oxygen generation and H_2O_2 concentration. d–f) Antiproliferative activity (IC_{50}) of AS1411 derivatives in (d) MCF-10A cells and (e,f) 4T1 cells treated for 96 h. g) Apoptosis analysis using annexin V-FITC/PI double staining on 4T1 cells either untreated or treated for 96 h with 10 μM AS1411 derivatives (the proportion of apoptotic cells was the sum of early and late apoptotic cells). h) Targeting 4T1 breast cancer cells with a fluorescently labelled AS1411-A (from left to right: DAPI and FAM channels, bright field and merged channels).

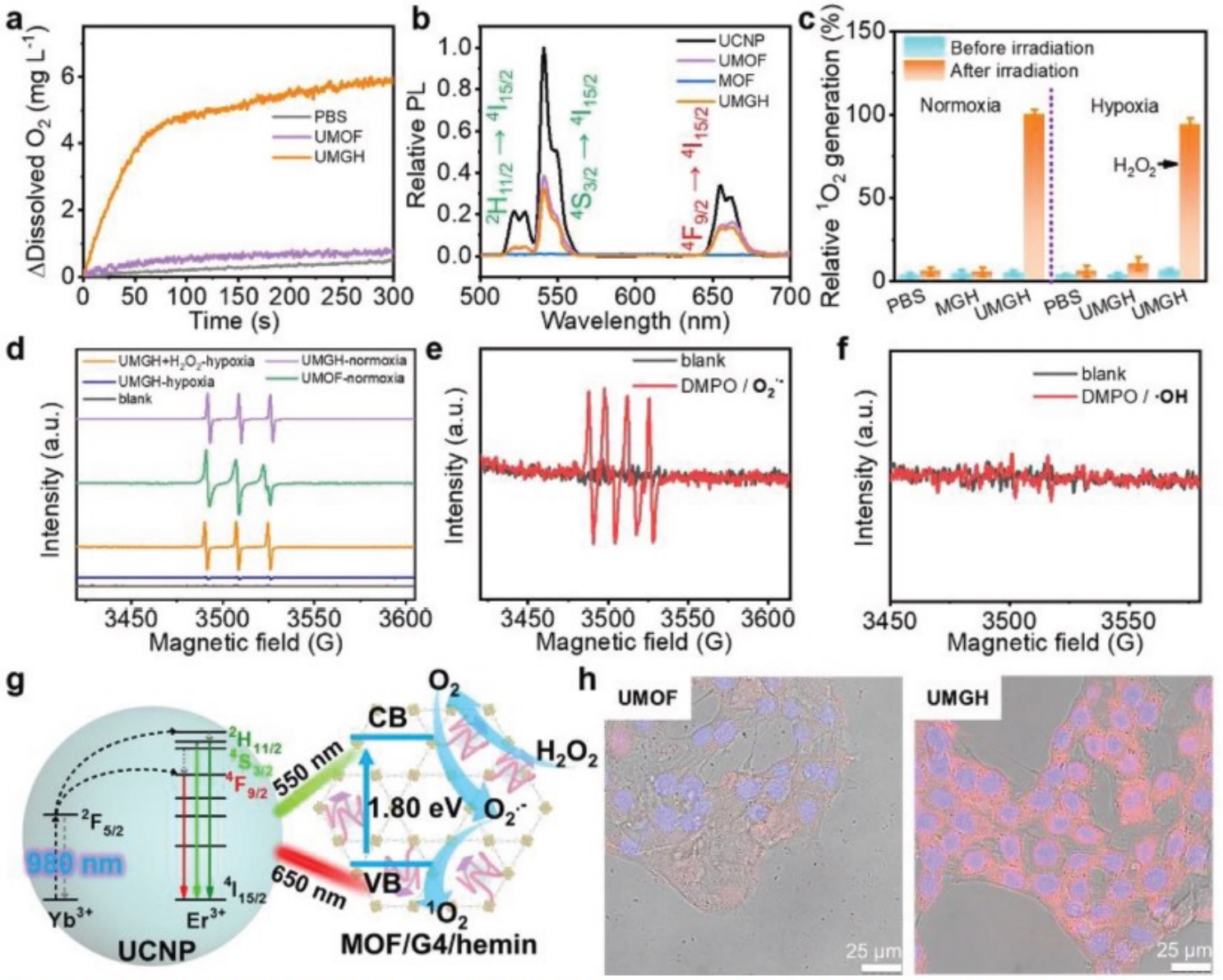

Figure 3. Characterizations of UMGH properties: a) O_2 generation in PBS solution without or with UMOF and UMGH in the presence of H_2O_2. b) Luminescence (UCL) emission of UCNP, MOF, UMOF and UMGH. c) Singlet oxygen ($^1O_2$) production detected by SOSG indicator under normoxia and hypoxia conditions before and after irradiation. d–f) Electron spin resonance (ESR) spectra of (d) TEMP-UMGH in aqueous suspension with or without H_2O_2 and (e,f) DMPO-H_2O_2-UMGH in (e) methanol solution and (f) aqueous solution, obtained after irradiation (980 nm) under N_2. g) Schematic illustration of the possible mechanism by which UMGH converted H_2O_2 to O_2 and then O_2 is converted to $^1O_2$ under NIR irradiation. h) Merged images showing the accumulation of UMOF and UMGH in 4T1 cells after incubation for 8 h at 37 °C. The corresponding images with Hoechst, UMGH and bright field are shown in Figure S19 (Supporting Information).

UMOF or UMGH, in accordance with the results depicted in Figure 3c. As seen in Figure 3e, four distinctive peaks (1:1:1:1 ratio) were observed in the spectrum of UMGH in the presence of 5,5-dimethyl-1-pyrroline N-oxide (DMPO) in MeOH solution containing 100 μM H_2O_2 upon irradiation of 980 nm laser for 30 min, confirming the generation of $O_2^{\bullet-}$ radicals. In contrast, a very faint signal was noticed in DMPO in an aqueous solution containing 100 μM H_2O_2, suggesting that the production of •OH radicals was minimal under these conditions (Figure 3f).

MOFs have emerged as promising photocatalysts activated by visible light as the metallic nodes of MOFs act as inorganic semiconductors and the bridging organic linkers serve as antennae to harvest light energy and transfer it to the metal clusters.[31] Given the semiconductor-like behavior of outer PCN-222 MOF shell in UMGH,[23a,31a,32] it is reasonable to assume that upon exposure to NIR light, photo-induced holes (h^+) and electron (e^-) may be generated. The light absorption measurement of UMGH was conducted using UV–vis diffuse reflectance spectroscopy (DRS) (Figure S17a, Supporting Information), which revealed the presence of Soret and Q bands belonging to the porphyrins. Since the UCNP core emitted green and red light, the band gaps energy (Eg) was determined to be ca. 1.80 eV from DRS spectrum using the Tauc plot method (Figure S17b, Supporting Information). Additionally, Figure S18 (Supporting Information) demonstrated that the valence band (VB) of UMOF was located at 0.87 eV in the XPS spectrum, and their conduction band (CB) was calculated to be −0.93 eV according to the empirical formula $E_{CB} = E_{VB} - Eg$, in agreement with previous findings.[23a] On this basis, we can postulate a mechanism (Figure 3g) for the catalytic production of $^1O_2$ by UMGH: we believe that the anchored GH complexes

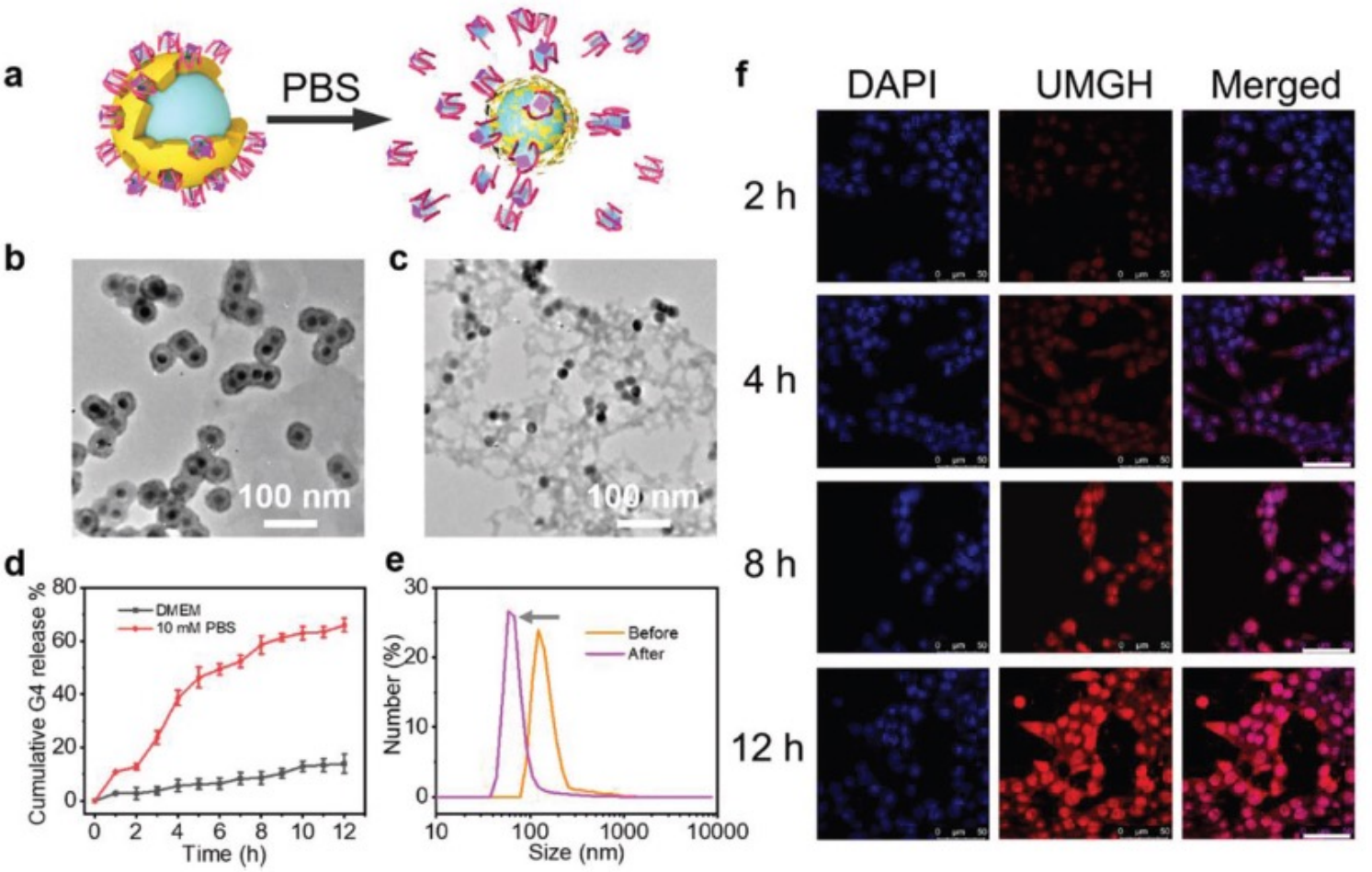

Figure 4. a) Schematic illustration of the degradation of UMGH in PBS and of the release of GH, which originates in the high affinity of Zr(IV) to phosphate ions. b and c) TEM images of UMGH before (b) and after (c) incubation with 10 mM PBS solution for 24 h. d) Degradation profiles of UMGH incubated in either DMEM or 10 mM PBS. e) Change in size of UMGH before (orange) and after (purple) a 24-h incubation in PBS. f) CLSM images showing the decomposition of UMGH after internalization in 4T1 cells (nuclei stained with DAPI; scale bars: 50 μm).

convert H_2O_2 into O_2 with high efficiency, which is itself converted into $^1O_2$ according to the following cascade: upon irradiation at 980 nm, the UCNP cores emitted green and red light, which is rapidly absorbed by the outer PCN-222 MOF shell, thus creating e^- and h^+ that migrate to the nanoparticle surface and collide with $O_2^{\bullet-}$ radicals (produced concomitantly with O_2) to produce $^1O_2$. The core-shell UMGH nanoplatform is thus anticipated to enhance PDT via the in situ generation of oxygen.

The ability of UMGH to target cancer cells was then investigated by optical imaging: as seen in Figure 3h and Figure S19 (Supporting Information), UMGH strongly accumulated in 4T1 cells compared to UMOF (red fluorescence), indicating that G4/hemin complexes endowed UMGH with good cancer cell targeting ability. The black dots visible in the UMOF image may be ascribed to its aggregation outside the cells, further indicating that the presence of GH complexes onto the surface of UMOF improved the stability of the resulting UMGH in DMEM medium. Altogether, these results showed that the UMGH nanoplatform can concomitantly trigger the catalytic degradation of H_2O_2 to produce O_2 and the conversion of O_2 into $^1O_2$ under 980 nm irradiation, and also be specific to cancer cells. This makes the UMGH nanoplatform a good candidate for further biological investigations.

2.4. Therapeutic Activation of UMGH by High Phosphate Concentration

From a strategic viewpoint, it could be advantageous for the UMGH to gradually degrade in order to liberate GH after its internalization. As illustrated in **Figure 4**a, UMGH is indeed expected to degrade in the presence of PBS due to the high affinity of Zr(IV) for phosphate ions, which associate to form a low solubility adduct ($K_{sp} = 10^{-134}$).[33] TEM images (Figures 4b,c) confirmed that UMGH degraded over 24 h in 10 mM PBS, while it remained stable in the absence of PBS. This degradation was found to be faster in PBS solution than in DMEM (Figure 4d). This was confirmed by DLS results, which showed that the hydrodynamic size of UMGH markedly decreased from 122 to 58 nm after being incubated in PBS for 24 h (Figure 4e).

We can thus speculate that in cells, UMGH could be degraded during endosomal trafficking, where the phosphate concentration is high. This is supported by CLSM images and an endosome/UMGH colocalization experiment (Figure 4f; Figure S20, Supporting Information): after a 3-h incubation of UMGH in 4T1 cells, a partial overlap of green (lysotracker, lysosome) and red (UMGH) signals indicated partial colocalization (Figure S20, Supporting Information). As seen in Figure 4f, the UMGH

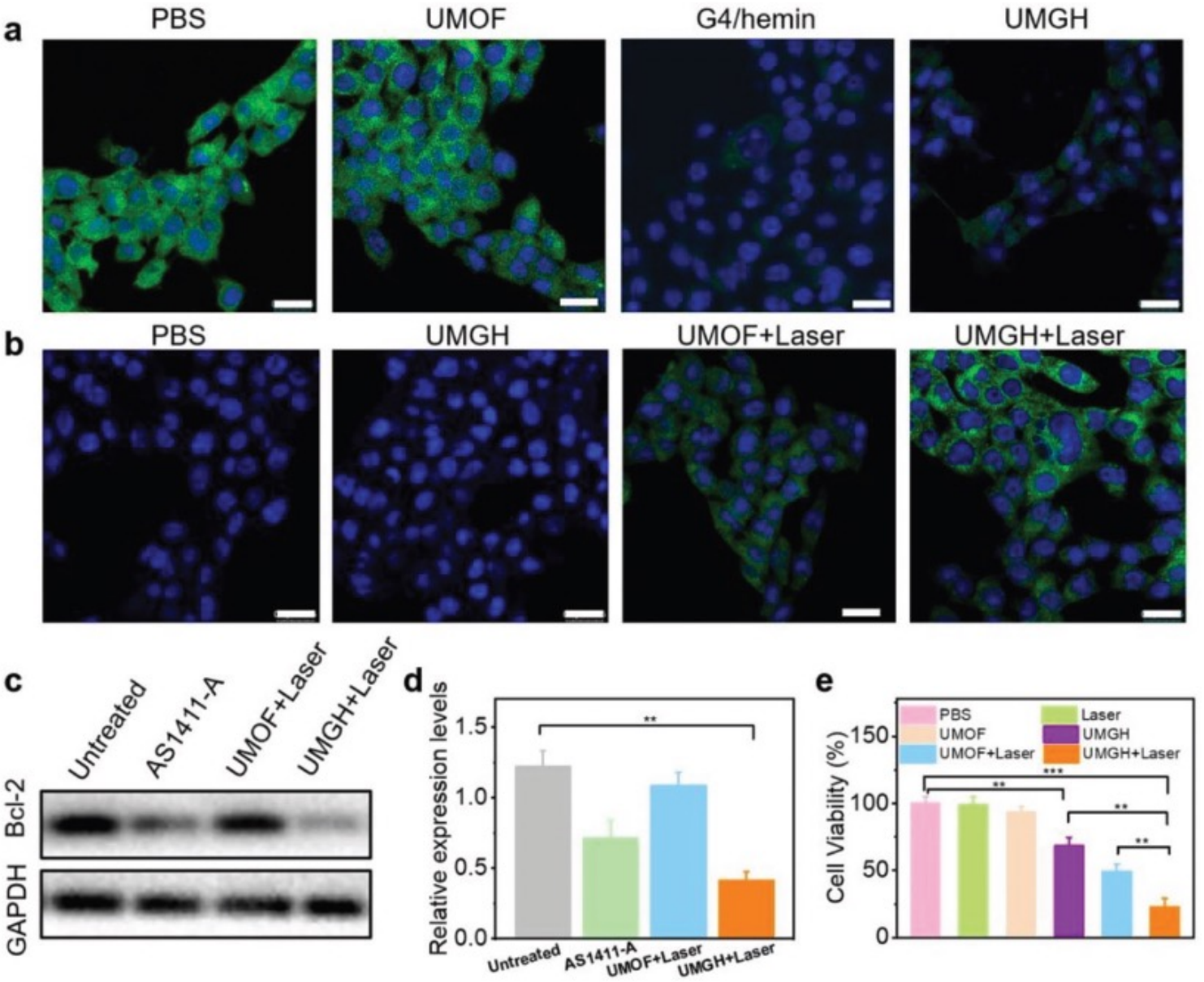

Figure 5. In vitro studies of UMGH nanoplatform. a, b) Intracellular O_2 (a) and $^1O_2$ (b) generation by UMOF, GH, and UMGH with or without 980 nm irradiation: green signals corresponded to image-iT™ hypoxia reagent (a) and SOSG singlet oxygen indicator (b) (nuclei stained with DAPI; scale bars: 25 μm). c, d) Western blot (c) and quantified Bcl-2 expression levels (d) from 4T1 cells under different treatments (GAPDH used as internal reference). e) In vitro evaluation of PDT and antiproliferative activity of UMOF and UMGH in 4T1 cells (MTT assay), with and without 980 nm irradiation (0.5 W cm^{-2} for 30 min). **$p < 0.01$, ***$p < 0.001$.

nanoplatform is stable in endosomes for 4 h; this is why we decided to expose cells to NIR light (980 nm) for 4 h after the start of the UMGH incubation in subsequent experiments.

2.5. In Vitro Therapy of UMGH

To go a step further, the concentration of O_2 in 4T1 cells incubated with UMGH under hypoxic conditions was assessed using the image-iT™ green hypoxia reagent: as seen in **Figure 5**a, both PBS- and UMOF-treated cells exhibited strong green fluorescence; in contrast, after incubation with either GH or UMGH, the fluorescence intensity was strongly decreased, indicating that GH and UMGH were indeed capable of diminishing hypoxia in cells. The generation of intracellular $^1O_2$ was estimated by CLSM imaging (Figure 5b): a bright green fluorescence was observed with UMGH- and UMOF-treated cells upon 980-nm irradiation only, the former being far higher than the latter, indicating the involvement of GH in the conversion of H_2O_2 into O_2.

As discussed above, part of the AS1411 anticancer activity results from a lowered expression of the Bcl-2 protein.[9,18] To verify whether AS1411-A acts in a similar manner, we performed immunoblotting experiments (with GAPDH as internal reference) to measure the expression of Bcl-2 in 4T1 cells upon several treatments. Results seen in Figures 5c,d demonstrated that 4T1 cells incubated with UMOF under NIR irradiation (980 nm) exhibited a slight decrease in Bcl-2 expression, while cells incubated with AS1411-A showed a more significant decrease (ca. 58% of the untreated group); similarly, cells incubated with UMGH experienced a pronounced reduction of Bcl-2 expression following 980 nm light exposure. Additionally, MTT assays were performed to confirm the lack of toxicity of UMOF (cell viability >

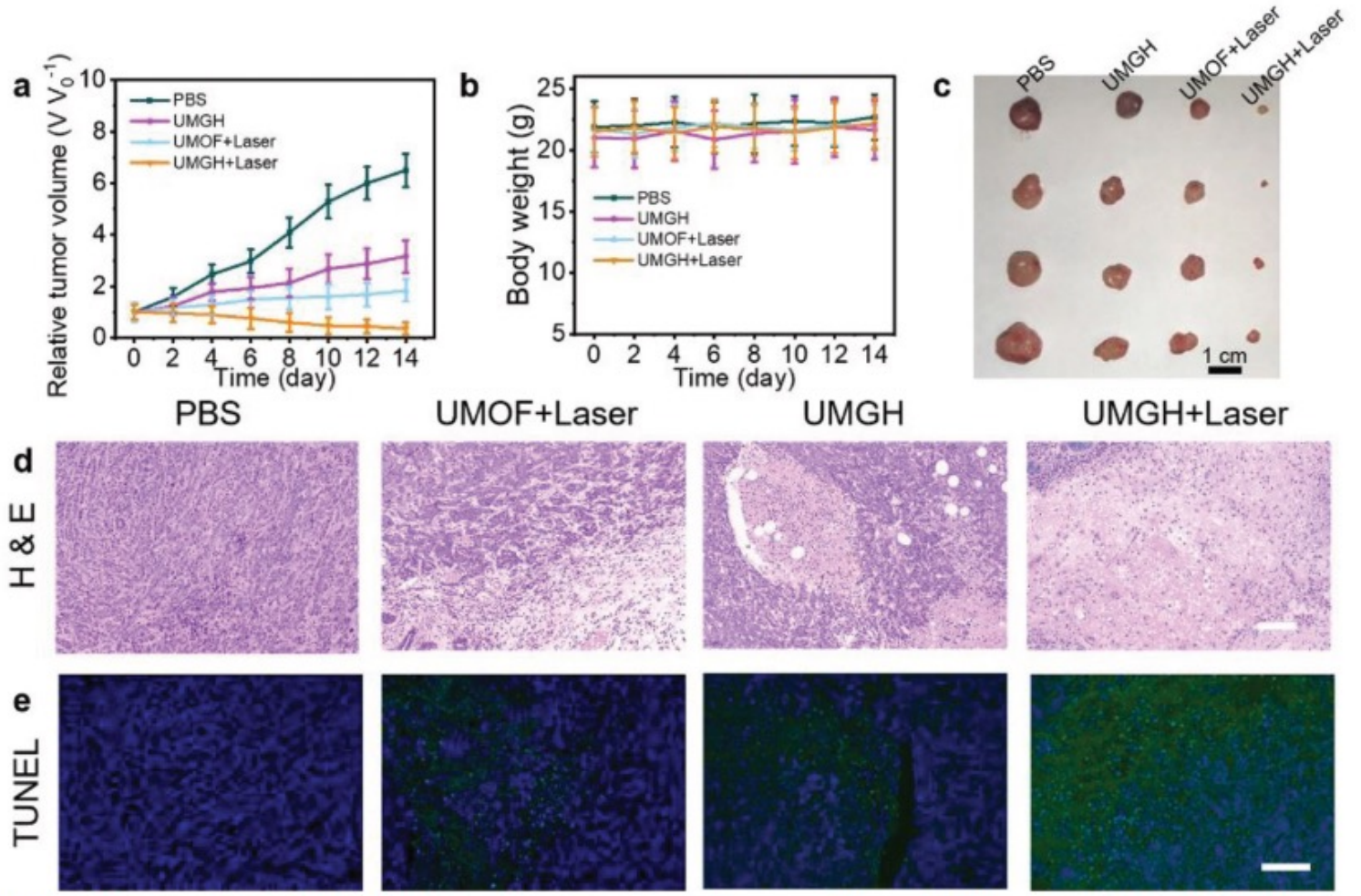

Figure 6. Therapeutic effect of UMGH after intratumoral injection in mice. a-c) Tumor growth curves (a) and body weight changes (b) of 4T1 tumor-bearing BALB/c mice under different treatments for 14 days. c) Images of tumors collected from 4 groups of mice after different treatments for 14 days. d, e) H&E stained images (d) and (e) TUNEL assays of tumor slices collected from 4T1 tumor-bearing mice treated with PBS, UMOF and irradiation, UMGH, UMGH and irradiation (scale bars: 100 μm).

93%, Figure S21a, Supporting Information) and the antiproliferative activity of GH (100 μg mL^{-1} UMGH triggered a decrease to 69% of cell viability) for 4T1 cells. In contrast, UMGH had no significant toxicity to MCF-10A cells (Figure S21b, Supporting Information) owing to the lack of targeting effect. We also observed that NIR irradiation enhanced UMGH toxicity (Figure 5e): while the 980-nm irradiation and the incubation of UMOF did not display any toxicity, a 30-min irradiation of cells incubated with UMGH triggered ca. 77% of cell death (versus 51% for cells incubated with UMOF). Collectively, these results showed that UMGH could exert its anticancer properties through a combination of ROS production, hypoxia attenuation, and GH antiproliferative activity.

2.6. In Vivo Therapy of UMGH

Taking into account the promising in vitro results of UMGH against 4T1 cell proliferation, its antiproliferative activity was evaluated on tumor-bearing mice through intratumoral injection. After collecting the feces and urine for 6 days after injection of UMGH, ICP-MS analyses showed that 72.6% of Y and 75.9% of Zr were excreted through feces and urine, respectively, confirming the degradation of UMGH (Figure S22a,b, Supporting Information). In comparison to UMOF, Y and Zr accumulation in tumor one day post-injection of UMGH were much higher, demonstrating the tumor targeting ability of UMGH (Figure S22c, Supporting Information). We then monitored the tumor volume over a period of 14 days after different treatments: as seen in **Figure 6**a, the relative tumor volume in mice treated with either UMGH without laser irradiation or UMOF after laser illumination was 48% and 29% of that of the control (PBS), confirming the antiproliferative effect of GH within UMGH and of the PDT mediated by UMOF itself. The tumors in mice treated with UMGH and irradiated were nearly eliminated (decreasing to 5% after 14 days), confirming that UMGH displayed enhanced, multifactorial antiproliferative activity. The survival rate of mice treated with UMGH and laser irradiation was higher than for other groups (Figure S22d, Supporting Information). No noticeable change in body weight was observed during the treatment, indicating its safety (Figure 6b). This remarkable antitumor effect was corroborated by the size of the tumors that were surgically removed from mice in every group (Figure 6c).

We also evaluated the expression of Bcl-2 in tumor slices by a Bcl-2 staining assay (Figure S23a, Supporting Information): the PBS-treated mice and those treated with UMOF with

irradiation exhibited strong and bright Bcl-2 foci whereas those treated with UMGH without irradiation and UMGH with irradiation displayed weak immunofluorescence only, indicating reduced Bcl-2 levels. We also assessed the changes in hypoxia tracking the transcription factor hypoxia-inducible factor 1-alpha (HIF-1α, Figure S23b, Supporting Information): strong immunofluorescence signals were seen within the PBS-treated and UMOF-treated cells with irradiation, while a low immunofluorescence was observed within those treated with UMGH without irradiation and UMGH upon irradiation, demonstrating that higher O_2 concentrations relieved tumor hypoxia.

Hematoxylin and eosin (H&E) staining experiments were also performed with tumor slices (Figure 6d) to illustrate the damage triggered by incubation with UMGH, UMOF, and UMGH upon laser irradiation, which was especially serious in the UMGH group. Terminal deoxynucleotidyl transferase mediated dUTP-biotin nick end labeling (TUNEL) staining experiments (Figure 6e) confirmed these results, showing that the UMGH-treated group with irradiation had the highest apoptosis level.[18,22b] Both H&E and TUNEL results could explain the drastic decrease of the tumor size after intratumoral injection of UMGH, which mediated its activity through strengthened PDT and antiproliferative activity of released AS1411-A, which translated into the tumor growth curves seen in Figure 6a. Furthermore, the lack of apparent pathological abnormalities within other major organs (Figure S24, Supporting Information) reaffirmed the potential of UMGH as a PDT agent.

3. Conclusion

In this study, we designed, synthesized and studied a novel G4/hemin (GH) complex that displayed enhanced capacity for catalytically converting H_2O_2 into O_2, stabilizing nanoparticles, targeting cancer cells and killing them via an apoptotic pathway. Then, the upconverted MOF (UMOF) was decorated with GH complexes and the resulting core-shell UMGH nanoplatform was used to catalyze O_2 formation from H_2O_2 and further catalyze the generation of $^1O_2$ upon 980 nm NIR irradiation, which was responsible for the enhanced photodynamic therapeutic (PDT) activity of UMGH. Further, the grafted GH within UMGH endowed it with improved chemical stability, chemotherapeutic activity, enhanced O_2 generation and targeting tumor ability. Compared to recently reported platforms, the UMGH system developed here has the advantages of being easily synthesized, at minimal cost. The chemotherapeutic activity and enhanced PDT of UMGH were validated both in vitro and in vivo, and these results clearly showed that UMGH display remarkable antitumor properties. This work thus provides a new landmark in the development of G4-based nanomedicine.

4. Experimental Section

The main experimental procedures were introduced here, while other protocols were shown in the supporting information.

UMGH Synthesis: The synthesis method of UMGH was based on the reported method with several modifications.[3b] Specifically, 2 mL of 1 mg mL^{-1} prepared UMOF was dispersed into 2 mL 10 μM G4/hemin solution, with vigorous stirring at room temperature for 24 h. Subsequently, the products were centrifugated and washed three times with water. Ultimately, the obtained products were redispersed in water with 100 mM KCl for subsequent uses.

Catalyzing the Decomposition of H_2O_2 to Generate O_2: The O_2 concentration in PBS buffer solution was recorded in real time in the presence of different products including AS1411/hemin complexes with different AS1411 derivatives, UMOF and UMGH. Briefly, these compounds were added in 2.0 mM H_2O_2 respectively, followed by N_2 blowing for 30 min. The generated O_2 concentration was immediately monitored by a dissolved O_2 analyzer, using a mixture of PBS and H_2O_2 as control.

Intracellular Oxygen Generation by UMGH: Image-iT green hypoxia reagent, whose fluorescence was quenched by O_2 in live cells and tissues, was used as O_2 indicator to monitor the O_2 production with UMGH. Briefly, 4T1 cells were pretreated with fresh culture medium containing UMOF and UMGH for 24 h in hypoxia environment and then the medium was replaced with 5 μM image-iT green hypoxia reagent for another 0.5 h. Then, confocal fluorescence images were collected between 510 and 540 nm under an excitation at 488 nm.

Antiproliferative Activity Test of AS1411 Derivatives: The antiproliferative effect of AS1411 derivatives was evaluated using typical MTT assays. For the analysis, 4T1 cells were plated in 96-well plates with 5.0×10^4 cells in each well and incubated for 24 h at 37 °C. The 4T1 cells were then incubated with fresh DMEM medium containing 10 μM AS1411 derivatives for another 96 h. Then, 50 μL of MTT stock solution (2 mg mL^{-1}) were added to each well and incubated for another 4 h. Next, 150 μL DMSO were added to dissolve the precipitated formazan after removing the culture medium. The absorbance at 490 nm was monitored on a microplate reader, all samples being prepared in triplicate.

In Vivo Anticancer Effect in a Subcutaneous Model: All animal assays were conducted in agreement with the NIH guidelines for the care and use of laboratory animals (NIH Publication no. 85-23 Rev. 1985) and approved by the experimental animal center of Nanjing University of Chinese Medicine (Approval Number: 202208A041). To establish a 4T1 tumor xenograft mouse model, female BALB/c mice (6–8 weeks-old) were inoculated with 4T1 cells (1.0×10^6) subcutaneously into the right flank position. After the tumor size reached 70–90 mm^3, 4T1 tumor bearing mice were randomly divided into four groups and treated as follows: i) PBS, ii) UMGH, iii) UMOF with laser irradiation, iv) UMGH with laser irradiation. UMOF and UMGH were injected intratumorally at a concentration of 2 mg mL^{-1}. In the experiments, tumors at 4 h post-injection were irradiated by the 980 nm laser (0.6 W cm^{-2}) for 30 min with 5 min breaks after every 5 min irradiation. The injection and treatment were repeated with the same procedure on days 2, 4, 8, and 12. Tumor size was measured with a vernier caliper every two days and calculated by the formula (length × width × width)/2. The body weight of each mouse was recorded every 2 days. Tumors and major organs (heart, liver, spleen, lung, and kidney) were sectioned for hematoxylin-eosin staining (H&E), TUNEL analysis and immunefluorescence analyses at the end of the experiment.

Acknowledgements

X.M. and X.Z. are joint first authors. The authors acknowledge the financial support of the National Natural Science Foundation of China (21977045, 22177047, 22004062, and 22104063), the Fundamental Research Funds for the Central Universities (020514380299, 202200324, and 202200325), State Key Laboratory of Analytical Chemistry for Life Science (5431ZZXM2202 and SKLACLS2109, SKLACLS2307), China Postdoctoral Science Foundation (2021M702106), Agence Nationale de la Recherche (ANR G4Access [ANR-20-CE12-0023]) and INCa PL-Bio (G4Access).

Conflict of Interest

The authors declare no conflict of interest.

Data Availability Statement

The data that support the findings of this study are available from the corresponding author upon reasonable request.

Keywords

antiproliferative activity, G-quadruplex, G-quadruplex/hemin, photodynamic therapy, upconverted metal-organic frameworks

Received: May 12, 2023
Revised: July 3, 2023
Published online:

[1] J. L. Mergny, D. Sen, *Chem. Rev.* **2019**, *119*, 6290.

[2] a) E. Y. N. Lam, D. Beraldi, D. Tannahill, S. Balasubramanian, *Nat. Commun.* **2013**, *4*, 1796; b) H. Y. Liu, Q. Zhao, T. P. Zhang, Y. Wu, Y. X. Xiong, S. K. Wang, Y. L. Ge, J. H. He, P. Lv, T. M. Ou, J. H. Tan, D. Li, L. Q. Gu, J. Ren, Y. Zhao, Z. S. Huang, *Chem. Biol.* **2016**, *23*, 1261; c) G. Biffi, D. Tannahill, J. Miller, W. J. Howat, S. Balasubramanian, *PLoS One* **2014**, *9*, e102711; d) R. Hansel-Hertsch, D. Beraldi, S. V. Lensing, G. Marsico, K. Zyner, A. Parry, M. D. Antonio, J. Pike, H. Kimura, M. Narita, D. Tannahill, S. Balasubramanian, *Nat. Genet.* **2016**, *48*, 1267; e) J. Spiegel, S. Adhikari, S. Balasubramanian, *Trends Chem.* **2020**, *2*, 123.

[3] a) A. Abiri, M. Lavigne, M. Rezaei, S. Nikzad, P. Zare, J. L. Mergny, H. R. Rahimi, *Pharmacol. Rev.* **2021**, *73*, 897; b) X. X. Mao, F. N. He, D. H. Qiu, S. J. Wei, R. G. Luo, Y. Chen, X. B. Zhang, J. P. Lei, D. Monchaud, J. L. Mergny, H. X. Ju, J. Zhou, *Anal. Chem.* **2022**, *94*, 7295.

[4] a) C. R. Ireson, L. R. Kelland, *Mol. Cancer Ther.* **2006**, *5*, 2957; b) P. J. Bates, D. A. Laber, D. M. Miller, S. D. Thomas, J. O. Trent, *Exp. Mol. Pathol.* **2009**, *86*, 151. c) P. J. Bates, E. M. Reyes-Reyes, M. T. Malik, E. M. Murphy, M. G. O. Toole, J. O. Trent, *Biochim. Biophys. Acta, Gen. Subj.* **2017**, *1861*, 1414. d) R. Yazdian-Robati, P. Bayat, F. Oroojalian, M. Zargari, M. Ramezani, S. M. Taghdisi, K. Abnous, *Int. J. Biol. Macromol.* **2020**, *155*, 1420.

[5] C. Riccardi, E. Napolitano, C. Platella, D. Musumeci, D. Montesarchio, *Pharmacol. Ther.* **2021**, *217*, 107649.

[6] E. M. Garcia-Recio, C. Pinto-Diez, M. I. Perez-Morgado, M. Garcia-Hernandez, G. Fernandez, M. E. Martin, V. M. Gonzalez, *Mol. Ther. Nucleic Acids* **2016**, *5*, e275.

[7] J. Hu, Z. L. Zhao, Q. L. Liu, M. Ye, B. Q. Hu, J. Wang, W. H. Tan, *Chem. Asian J.* **2015**, *10*, 1519.

[8] a) N. Q. Do, W. J. Chung, T. H. A. Truong, B. Heddi, A. T. Phan, *Nucleic Acids Res.* **2017**, *45*, 7487; b) T. K. Sengupta, S. Bandyopadhyay, D. J. Fernandes, E. K. Spicer, *J. Biol. Chem.* **2004**, *279*, 10855; c) Y. Otake, T. K. Sengupta, S. Bandyopadhyay, E. K. Spicer, D. J. Fernandes, *Mol. Pharmacol.* **2005**, *67*, 319; d) S. Soundararajan, W. W. Chen, E. K. Spicer, N. Courtenay-Luck, D. J. Fernandes, *Cancer Res.* **2008**, *68*, 2358.

[9] a) J. Carvalho, J. L. Mergny, G. F. Salgado, J. A. Queiroz, C. Cruz, *Trends Mol. Med.* **2020**, *26*, 848; b) C. Roxo, W. Kotkowiak, A. Pasternak, *Molecules* **2019**, *24*, 3781.

[10] a) D. Q. Fan, J. Wang, E. K. Wang, S. J. Dong, *Adv. Sci.* **2020**, *7*, 2001766; b) H. X. Zhao, L. H. Li, F. Li, C. X. Liu, M. X. Huang, J. Li, F. Gao, X. H. Ruan, D. Y. Yang, *Adv. Mater.* **2022**, *34*, 2109920; c) J. J. Shi, W. M. Nie, X. Zhao, X. Y. Yang, H. Cheng, T. H. Zhou, Y. Zhang, K. X. Zhang, J. J. Liu, *Adv. Mater.* **2022**, *34*, 2201049.

[11] a) P. H. Tong, L. Zhu, Y. Zhang, J. Li, X. P. He, T. D. James, *Chem. Commun.* **2021**, *57*, 12098; b) S. Q. Dong, Q. X. Chen, W. Li, Z. Jiang, J. B. Maa, H. Gao, *J. Mater. Chem. B* **2017**, *5*, 8322; c) S. Mallakpour, E. Nikkhoo, C. M. Hussain, *Coord. Chem. Rev.* **2022**, *451*, 214262. d) B. Liu, M. Jiang, D. Z. Zhu, J. M. Zhang, G. Wei, *Chem. Eng. J.* **2022**, *428*, 131118.

[12] a) J. C. Yan, T. Gao, Z. Z. Lu, J. B. Yin, Y. Zhang, R. J. Pei, *ACS Appl. Mater. Interfaces* **2021**, *13*, 27749; b) X. Zhao, K. X. Zhang, Y. Y. Wang, W. X. Jiang, H. Cheng, Q. W. Wang, T. T. Xiang, Z. Z. Zhang, J. J. Liu, J. J. Shi, *Adv. Funct. Mater.* **2022**, *32*, 2108883. c) W. Morris, W. Briley, E. Auyeung, M. Cabezas, C. A. Mirkin, *J. Am. Chem. Soc.* **2014**, *136*, 7261;

[13] a) W. Zhang, J. Lu, X. Gao, P. Li, W. Zhang, Y. Ma, H. Wang, B. Tang, *Angew. Chem., Int. Ed.* **2018**, *57*, 4891; b) Y. Ma, X. Y. Li, A. J. Li, P. Yang, C. Y. Zhang, B. Tang, *Angew. Chem., Int. Ed.* **2017**, *56*, 13752; c) J. Park, Q. Jiang, D. W. Feng, L. Q. Mao, H. C. Zhou, *J. Am. Chem. Soc.* **2016**, *138*, 3518.

[14] a) K. R. Deng, C. X. Li, S. S. Huang, B. G. Xing, D. Y. Jin, Q. G. Zeng, Z. Y. Hou, J. Lin, *Small* **2017**, *13*, 1702299; b) Y. Z. Shen, A. J. Shuhendler, D. J. Ye, J. J. Xu, H. Y. Chen, *Chem. Soc. Rev.* **2016**, *45*, 6725.

[15] T. X. Gu, L. Cheng, F. Gong, J. Xu, X. Li, G. R. Han, Z. Liu, *ACS Appl. Mater. Interfaces* **2018**, *10*, 15494.

[16] a) X. S. Li, N. Kwon, T. Guo, Z. Liu, J. Yoon, *Angew. Chem., Int. Ed.* **2018**, *57*, 11522; b) L. Huang, S. Zhao, J. Wu, L. Yu, N. Singh, K. Yang, M. H. Lan, P. F. Wang, J. S. Kim, *Coordin. Chem. Rev.* **2021**, *438*, 213888.

[17] a) Y. L. Wan, L. H. Fu, C. Y. Li, J. Lin, P. Huang, *Adv. Mater.* **2021**, *33*, 2103978. b) L. R. Zhao, C. H. Fu, L. F. Tan, T. Li, H. S. Zhong, X. W. Meng, *Nanoscale* **2020**, *12*, 2855. c) D. Hu, L. Zhong, M. Wang, H. Li, Y. Qu, Q. Liu, R. Han, L. Yuan, K. Shi, J. Peng, Z. Qian, *Adv. Funct. Mater.* **2019**, *29*, 1806199. d) Z. F. Ma, M. C. Zhang, X. D. Jia, J. Bai, Y. D. Ruan, C. Wang, X. P. Sun, X. Jiang, *Small* **2016**, *12*, 5477. e) J. Zhou, M. H. Li, Y. H. Hou, Z. Luo, Q. F. Chen, H. X. Cao, R. L. Huo, C. C. Xue, L. Sutrisno, L. Hao, Y. Cao, H. T. Ran, L. Lu, K. Li, K. Y. Cai, *ACS Nano* **2018**, *12*, 2858. f) F. Hu, D. Mao, Kenry, Y. X. Wang, W. B. Wu, D. Zhao, D. L. Kong, B. Liu, *Adv. Funct. Mater.* **2018**, *28*, 1707519. g) X. S. Wang, J. Y. Zeng, M. K. Zhang, X. Zeng, X. Z. Zhang, *Adv. Funct. Mater.* **2018**, *28*, 1801783. h) J. P. Wang, J. Y. Sun, W. Hu, Y. H. Wang, T. Chou, B. L. Zhang, Q. Zhang, L. Ren, H. J. Wang, *Adv. Mater.* **2020**, *32*, 2001862.

[18] Y. Yang, W. J. Zhu, L. Z. Feng, Y. Chao, X. Yi, Z. L. Dong, K. Yang, W. H. Tan, Z. Liu, M. W. Chen, *Nano Lett.* **2018**, *18*, 6867.

[19] Y. Liu, Y. Yang, Y. J. Sun, J. B. Song, N. G. Rudawski, X. Y. Chen, W. H. Tan, *J. Am. Chem. Soc.* **2019**, *141*, 7407.

[20] A. G. Dong, X. C. Ye, J. Chen, Y. J. Kang, T. Gordon, J. M. Kikkawa, C. B. Murray, *J. Am. Chem. Soc.* **2011**, *133*, 998.

[21] S. Z. Wang, C. M. McGuirk, M. B. Ross, S. Y. Wang, P. C. Chen, H. Xing, Y. Liu, C. A. Mirkin, *J. Am. Chem. Soc.* **2017**, *139*, 9827.

[22] a) D. W. Feng, Z. Y. Gu, J. R. Li, H. L. Jiang, Z. W. Wei, H. C. Zhou, *Angew. Chem.* **2012**, *124*, 10453. b) L. C. He, Q. Q. Ni, J. Mu, W. P. Fan, L. Liu, Z. T. Wang, L. Li, W. Tang, Y. J. Liu, Y. Y. Cheng, L. G. Tang, Z. Yang, Y. Liu, J. H. Zou, W. J. Yang, O. Jacobson, F. Zhang, P. T. Huang, X. Y. Chen, *J. Am. Chem. Soc.* **2020**, *142*, 6822.

[23] a) W. L. Sheng, X. X. Wang, Y. X. Wang, S. L. Chen, X. J. Lang, *ACS Catal.* **2022**, *12*, 11078. b) J. H. Wang, Y. D. Fan, Y. H. Tan, X. Zhao, Y. Zhang, C. M. Cheng, M. Yang, *ACS Appl. Mater. Interfaces* **2018**, *10*, 36615. c) L. Gomathi Devi, P. M. Nithya, *Inorg. Chem. Front.* **2018**, *5*, 127.

[24] a) K. H. Yu, T. X. Wei, Z. J. Li, J. Y. Li, Z. Y. Wang, Z. H. Dai, *J. Am. Chem. Soc.* **2020**, *142*, 21267. b) A. E. Baumann, X. Han, M. M. Butala, V. S. Thoi, *J. Am. Chem. Soc.* **2019**, *141*, 17891.

[25] Z. X. Liang, H. Y. Song, S. J. Liao, *J. Phys. Chem. C* **2011**, *115*, 2604;

[26] S. Sen, V. Govindarajan, C. J. Pelliccione, J. Wang, D. J. Miller, E. V. Timofeeva, *ACS Appl. Mater. Interfaces* **2015**, *7*, 20538.

[27] a) G. X. Lan, K. Y. Ni, Z. W. Xu, S. S. Veroneau, Y. Song, W. B. Lin, *J. Am. Chem. Soc.* **2018**, *140*, 5670; b) Y. Zang, J. P. Lei, L. Zhang, H. X.

Ju, *Anal. Chem.* **2014**, *86*, 12362; c) R. Freeman, X. Q. Liu, I. Willner, *J. Am. Chem. Soc.* **2011**, *133*, 11597. d) M. M. Dailey, M. C. Miller, P. J. Bates, A. N. Lane, J. O. Trent, *Nucleic Acids Res.* **2010**, *38*, 4877.

[28] a) C. Riccardi, D. Musumeci, I. R. Krauss, M. Piccolo, C. Irace, L. Paduano, D. Montesarchio, *Int. J. Biol. Macromol.* **2018**, *118*, 1384. b) E. E. Iwaniuk, T. Adebayo, S. Coleman, C. G. Villaros, I. V. Nesterova, *Nucleic Acids Res.* **2023**, *51*, 1600.

[29] F. Wang, X. G. Liu, *J. Am. Chem. Soc.* **2008**, *130*, 5642.

[30] L. Zhang, J. P. Lei, F. J. Ma, P. H. Ling, J. T. Liu, H. X. Ju, *Chem. Commun.* **2015**, *51*, 10831.

[31] a) H. Q. Xu, J. H. Hu, D. K. Wang, Z. H. Li, Q. Zhang, Y. Luo, S. H. Yu, H. L. Jiang, *J. Am. Chem. Soc.* **2015**, *137*, 13440. b) M. Alvaro, E. Carbonell, B. Ferrer, F. X. Llabrés i Xamena, H. Garcia, *Chemistry* **2007**, *13*, 5106. c) T. Tachikawa, J. R. Choi, M. Fujitsuka, T. Majima, *J. Phys. Chem. C* **2008**, *112*, 14090.

[32] a) C. Y. Xu, H. Liu, D. D. Li, J. H. Su, H. L. Jiang, *Chem. Sci.* **2018**, *9*, 3152. b) Y. M. Zhao, Y. Z. Dong, F. T. Lu, C. G. Ju, L. Liu, J. Zhang, B. Zhang, Y. Q. Feng, *J. Mater. Chem. A* **2017**, *5*, 15380.

[33] C. B. He, K. D. Lu, D. M. Liu, W. B. Lin, *J. Am. Chem. Soc.* **2014**, *136*, 5181.